Review

Advances in laser-driven neutron sources and applications

A. Yogo[1,a], Y. Arikawa[1], Y. Abe[1], S. R. Mirfayzi[2], T. Hayakawa[3], K. Mima[1], R. Kodama[1]

[1] Institute of Laser Engineering, Osaka University, Suita, Osaka 565-0871, Japan
[2] Tokamak Energy Ltd, 173 Brook Dr, Milton, Abingdon OX14 4SD, UK
[3] National Institutes for Quantum and Radiological Science, and Technology, Tokai, Ibaraki 319-1106, Japan

Abstract Laser-driven neutron source (LDNS) is attracting interest for several reasons including (i) compactness of the source, (ii) neutron pulse shortness and (iii) transportability of laser beam. Through reviewing recent activities, we discuss the characteristics of LDNS in a comparison with accelerator-based neutron facilities (ABNF). Especially, we discuss the potential and limit of LDNS by showing that neutrons ranging from meV to MeV in energy were generated by LDNS and applied to neutron analysis and fundamental science.

1 Introduction

The evolution of laser and accelerator technologies have taken a new turn, giving rise to a new trans-disciplinary field termed by Nuclear Photonics. The advances in high-intensity laser technologies have also made it possible to accelerate GeV-class electrons [1] and near-100-MeV protons [2] from an area of less than 1 mm. Most importantly, secondary radiations such as laser-driven neutron sources (LDNS) are attracting a lot of interests as a promising application of the laser particle acceleration.

LDNS is defined as the neutron source that is driven or triggered by laser-plasma interactions. Figure 1 shows the reactions [3] used to generate neutrons in LDNS and accelerator-based neutron facilities (ABNF) where one may find a few analogical points between LDNS and ABNF. The spallation nuclear reaction (a) is employed in ABNF generating high flux neutrons, including SNS: Spallation Neutron Source, ISIS neutron and muon source, and J-PARC: Japan Proton Accelerator Research Complex, where GeV-class protons are injected into heavy metal targets. The photo-nuclear reactions (b) and low-energy nuclear reactions (c) are employed

by relatively compact accelerators of electrons and ions, respectively.

The developments of LDNS was started by studies in nuclear fusion reactions (d) [4–6], and later expanded to utilize the laser-accelerated particles (ion [7–25] or electron [26–28]) as the primary beam to generate neutrons via reactions (b) and (c). The physical background of the laser particle acceleration is discussed elsewhere in this special issue. The spallation (a) is not yet applied to LDNS because of the requirement of GeV protons.

The characteristics of LDNS have been demonstrated in several works: (i) the compactness of the source size ($\sim$ 1 cm), (ii) generating pulsed neutrons shorter than 1 ns at the source, and (iii) high transportability of laser light expanding the usable area of neutrons. However, it is still challenging to clarify the outstanding features that distinguish LDNS from ABNF. From the viewpoint of applications lower-energy neutrons are preferable, as discussed later, although the processes shown in Fig. 1 generates MeV neutrons. Accordingly, the method of decelerating the neutrons (moderation) is critical. However, the characteristics of LDNS, the compactness and the pulse shortness, are often canceled during the moderation process; hence, smart moderation techniques are required.

Neutrons exhibit very different properties depending on their kinetic energy. Neutrons produced in fusion and fission reactions ranges around MeV in energy and are termed by *fast* neutrons. Neutrons are statistically slowed down by the collisions with surrounding nuclei, and finally reach thermal equilibrium, having a continuous Boltzmann-like energy distribution. For example, thermalized neutrons with an average energy of keV predominantly govern the elemental synthesis reactions in the interiors of stars.

Fast neutrons are efficiently moderated by the scattering with the nuclei of light elements. Especially, the kinetic energy loss is maximized when the neutron scatters with a hydrogen nucleus. Lower energy neutrons, discussed in the

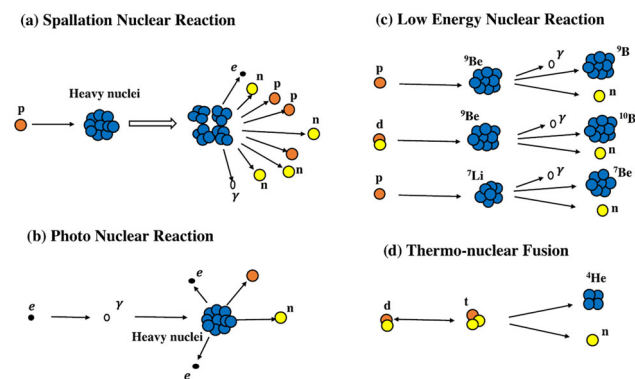[a] e-mail: yogo-a@ile.osaka-u.ac.jp (corresponding author)

Fig. 1 Neutron generation processes driven by accelerators and high-power lasers. **a** Spallation nuclear reaction, **b** photo-nuclear reaction, **c** low-energy nuclear reaction, **d** thermo-nuclear fusion. The figure was adopted from Ref. [3]

followings, are widely utilized for science and industry by moderating the fast neutrons with hydrogen-rich materials, including water and polymers.

The neutrons of typically 0.1–100 eV energies are termed *epi-thermal* neutrons. In this energy region, one of the most characteristic reactions is neutron resonance absorption. When the kinetic energy of a neutron coincides with an excited level of a nucleus, the neutron is resonantly absorbed by the nucleus, and the absorption occurs selectively in a very narrow energy range. After the reaction, the nucleus becomes unstable, and immediately emits γ-rays (prompt γ) and de-excited. By analyzing the energies of absorbed neutrons or prompt γ-rays, elemental and isotopic species can be identified.

When neutrons are slowed down by a material at room temperature ($\sim$ 300 K or 25 meV), they will be known as *thermal* neutrons. In general, the reaction probability of neutrons is inversely proportional to their velocity ($1/v$ law), so that thermal neutrons are absorbed by specific materials or scattered by light elements such as hydrogen with higher probabilities. This property is appropriate for radiographic analysis.

When neutrons are moderated down to $<$ 5 meV, they are termed by *cold* neutrons. In this case, the neutrons reveal their properties as waves. For example, the wavelength of a 1 meV neutron is about 9 Å, and can be used for the diffraction analysis of crystal structures of metals and proteins, when the sensitivity of neutrons to hydrogen are useful especially in the fields of life science, biology and medicine.

Nowadays, several groups [18,20–25] developed moderation systems for LDNS, and generated lower energy neutrons ranging from meV to MeV. The aim of this review is to share the activities of LDNS studies in the community and clarify the potentials and limits of them for applications. The overview of LDNS studies will be made in Sect. 2. In Sect. 3, we review recent results oriented to applications, focusing

on fast (3.1), epi-thermal (3.2), thermal (3.3) and cold (3.4) neutrons. The review is concluded in Sect. 4.

2 Overview of LDNS studies

Neutrons are regularly generated in laser-induced plasmas by large-scale laser facilities in the framework of inertial confinement fusion (ICF) research. At the National Ignition Facility about 200 laser beams of a few megajoule in total energy are employed for imploding the fuel target in nanosecond (ns) duration, leading to production of 10^{18} neutrons [29] as the yield of D-T fusion reaction. After the advent of the Chirped Pulse Amplification (CPA) technique [30], high-intensity short-pulse lasers also were introduced to the ICF researches. For instance, in 1988 photo nuclear neutrons were detected from the plasma induced by 10^{20} W cm^{-2}, 0.45 ps laser [5]. The neutron generation by relatively compact laser systems was reported in 1999 by Ditmire et al. [6], where a femtosecond (fs), sub-joule high intensity laser pulse was focused onto sub-mm-size deuterium cluster gas, and generated D-D fusion neutrons up to 10^4.

In 2000, several game-changing works [31–33] reported the acceleration of protons up to 10 s mega-electron volt (MeV) energies by lasers having the intensity exceeding 10^{18} W cm^{-2}. The mechanism is well known as target normal sheath acceleration (TNSA) [34]. When a high-intensity laser is focused onto a solid foil of a few micron thickness, plasma is induced by the rising foot of the laser pulse, Then, the electrons interact with the laser peak are accelerated up to relativistic energies ($>$ 0.511 MeV) via electro-magnetic processes, and swept out from the laser-irradiated (front) surface. The major part of the electrons are captured by the field on the backside of the target and pulled back, orbiting in the vicinity of the target. Accordingly, a charge separation field, termed by sheath, is generated on the target rear side. This sheath electric field is maintained during picosecond (ps) time scale and accelerates pulsed ions to the rear direction of the target.

The characteristic features of the ions by TNSA can be summarized as follows: (i) The acceleration is more predominant for ions having lower charge-to-mass ratio (q/M). In many cases, protons ($q/M = 1$) are accelerated most efficiently. (ii) The energy of accelerated ions exhibits a continuous distribution up to a cutoff (maximum) energy. The slope temperature and the cutoff energy are determined by the temperature of the plasma hot electrons. (iii) The ions are accelerated toward the normal direction of the rear surface with divergence angles inversely proportional to the ion energies. Typically, the half cone angle for protons having 50% energy of the cutoff is about 20° [35].

The LDNS utilizing the TNSA protons as the primary beam was reported in 2004 [7], where a block of lithium

fluoride (LiF) was located as a secondary target to generate neutrons via $^7\text{Li}(p, n)$ reaction. Recently, the LDNS research has been performed in several laser facilities all over the world, using proton or deuteron as primary beams combined with Li, beryllium (Be), or deuterated plastics. Table 1 shows the configurations of LDNS, the combination of targets, laser parameters and the resulting yield of neutrons generated per a laser shot.

A typical setup of the LDNS is shown in Fig. 2, where the energy spectra of accelerated ions and neutrons are simultaneously monitored in a single laser shot experiment. The energy of neutrons (Fig. 2c) shows a spectrum with the maximum value of 20 MeV, which is consistent with the cutoff energy of the protons (Fig. 2b). In addition, the slope temperatures are in agreement between the neutrons and the protons. These results are related to the breakup reaction as well as Q value which depends on the kinetic energy transfer from a proton to a neutron in the (p, n) reactions.

Figure 3 shows the neutron generation rate [36] for several kinds of secondary targets that are sufficiently thicker than the stopping range of incident ions. For Be target, the neutron generation rate is $\sim 4 \times 10^9$ n/μC and $\sim 2 \times 10^{10}$ n/μC typically for the beam of 5 MeV/u protons and deuterons, respectively. To enhance the neutron yield, Alejo et al. [17] developed a D_2O ice layer target system and succeeded in accelerating pure deuterons. Roth et al. [12] focused an ultrahigh-intensity laser (10^{21} W cm^{-2}) onto a thin (300 nm) deuterated plastic foil, resulting in pure deuteron acceleration up to 30 MeV/u via break-out afterburner (BOA), as a mechanism other than TNSA. The neutron yield obtained was 10^{10} with the (d, n) reactions. It was also reported [37] that lasers having longer pule duration 1–10 ps are favorable for the acceleration of heavier ions including deuterons.

Laser-accelerated electrons were also utilized to the LDNSs [26–28], where the fast electrons were converted into high energy γ-rays in order to generate neutrons via photonuclear reactions shown in Fig. 1b. Pomerantz et al. [26] accelerated MeV electrons by focusing a laser pulse onto an expanding plasma plume induced by low-level laser light arriving ~ 100 ns before the main laser pulse. The electrons were converted into γ-rays by a copper plate (18 mm in thickness) and generate neutrons by the $^{63}\text{Cu}(\gamma, n)^{62}\text{Cu}$ reaction. Günther et al. [27] enhanced the electron acceleration by using a plastic foam target, the plasma electron density of which is close to the critical density ($\sim 10^{21}$ cm^{-3}) for the 20 J, 10^{19} W cm^{-2} laser used in their experiment. The high energy electrons were injected into a high-Z thick metal and converted into neutrons of $\sim 10^{10}$ per a laser shot. Arikawa et al. [28] employed repetitive shots of a pair of high-intensity laser pulse. The first pulse dug a crater on a metal target, and consequently the second pulse was focused into the crater. The laser was reflected several times inside the crater, resulting in efficient electron generation.

The neutron yield per a unit energy of the laser was found to be $\sim 10^{8-9}$ neutrons/J for the LDNSs employing the low energy nuclear reaction (Fig. 1c). However, it is challenging to establish a universal scaling law on the neutron yields for a variety combination of primary and secondary targets, and laser parameters (energy, pulse duration, intensity, contrast ratio, and so on) which govern the ion acceleration mechanisms beside the nuclear reactions to generate neutrons. As a milestone, it was experimentally found that the neutron yield Y_n is proportional to the forth power of the laser intensity I_L [25]. In Fig. 4, the neutron yields observed by CR39 detectors (solid triangles) are in accordance with the yields (open triangles) predicted by the equation below:

$$Y_n = \frac{1}{4\pi} \sum_i \int_0^{E_{\max,i}} \frac{dN_i}{dE} R_i(E) dE. \tag{1}$$

Here, $\frac{dN_i}{dE} = \frac{dN_i}{dEd\Omega}\Omega(E/E_{\max,i})$ is the energy spectra of primary ion beams. $dN_i/dEd\Omega$ is the differential energy distribution of the ions and $\Omega(E/E_{\max,i})$ is the universal equation of ion divergence angle depending on the ion energy [35]. $R_i(E)$ is the neutron generation rate [36] when one ion is incident into a sufficiently thick secondary target. The yield is integrated over all ion species (i) injected into the secondary target. Under the condition that $R_i(E) \propto E^2$, the Eq. (1) is converted into

$$Y_n \propto I_L \sum_i E_{\max,i} \text{CE}_i, \tag{2}$$

where CE_i is the conversion efficiency from the laser energy ($\mathcal{E}_L$) into the total kinetic energies of ions, obtained by

$$\text{CE}_i = \frac{1}{\mathcal{E}_L} \sum_i \int_0^{E_{\max,i}} \frac{dN_i}{dE} E dE. \tag{3}$$

Detailed discussed was made in Ref. [25]. Note $\mathcal{E}_L \propto I_L$ when the pulse duration and the focal condition are fixed. As shown in Fig. 5a, b, it was experimentally found that $E_{\max,i} \propto I_L$ and $\text{CE}_i \propto I_L^2$ for i = proton and deuteron, justifying the $Y_n \propto I_L^4$ dependency in Fig. 4. In more general form, the neutron yield was scaled by

$$Y_n \propto I_L^{k+m+1}, \tag{4}$$

where k and m are the scaling parameters involved in $E_{\max,i} \propto I_L^k$ and $\text{CE}_i \propto I_L^m$, respectively.

3 Applications

3.1 Fast neutron

As discussed in Sect. 2, fast neutrons in the range of MeV energies are directly generated from LDNS. High energy neutrons can penetrate from several centimeters to meters

Table 1 The configurations of LDNS, the combination of targets, laser parameters and the resulting yield of neutrons generated per a laser shot. CD and CD_2 indicate deuterated polystyrene ($-C_8D_8-)_n$ and deuterated polyethylene ($-C_2D_4-)_n$, respectively

| Author	Reaction	Target Primary	Secondary	Laser configuration Energy [J]	Intensity [Wcm^{-2}]	Duration [ps]	Neutron yield [n/sr]	[n/sr/J]
Lancaster [7]	Li(p,n)Be	CH	LiF	80	3×10^{19}	1	3.0×10^8	3.75×10^6
Higginson [8]	Li(p,n)Be	Cu	LiF	140	1×10^{20}	0.7	1.0×10^8	7.1×10^5
Higginson [9]	Li(d,n)Be	CD_2	LiF	360	2×10^{19}	9	8.0×10^8	2.2×10^6
Willingale [10]	D(d,n)He	CD	CD	6	2.6×10^{19}	0.4	5.0×10^4	8.3×10^3
Jung [11]	Be(p,n)B, Be(d,n)	CD_2, CH	Be	80	5×10^{20}	0.6	4.4×10^9	5.5×10^7
Roth [12]	Be(p,n)B, Be(d,n)	CD_2	Be	80	5×10^{20}	0.6	5.0×10^9	6.3×10^7
Zulick [13]	Li(p,n)Be	CH_2	LiF	1.1	2×10^{21}	0.04	1.0×10^7	9.1×10^6
Maksimchuk [14]	D(d,n)He	D_2O ice on Cu	CD	6	2×10^{19}	0.4	4.0×10^5	6.7×10^4
Storm [15]	Li(p,n)Be	Si_3N_4	Li	60	2×10^{20}	0.18	1.6×10^7	2.7×10^5
Pomerantz [26]	photo-nuclear	plastic	Cu	90	-	0.15	1.0×10^7	1.1×10^5
Kar [16]	D(d,n)He	CD	CD	220	3×10^{20}		8.0×10^8	3.6×10^6
Alejo [17]	D(d,n)He	D_2O ice on Cu	CD	200	2×10^{20}	0.75	2.0×10^9	1.0×10^7
Kleinschmidt [19]	Be(p,n)B, Be(d,n)	CD	Be	175	2×10^{20}	0.5	1.42×10^{10}	8.1×10^7
Zimmer [24]	(p,n), (d,n)	foam + high-Z metals	LiF-Be	100	2×10^{20}	0.6	1.43×10^9	1.4×10^7
Günther [27]	photo-nuclear	foam + Au	–	20	$\sim 10^{19}$	0.75	1.11×10^9	5.5×10^7
	(p,n)	foam + Au	–	20	$\sim 10^{19}$	0.75	4.93×10^9	2.5×10^8
Yogo [25]	Be(p,n)B, Be(d,xn)	CD	Be	900	1×10^{19}	1.5	2.3×10^{10}	2.6×10^7
Arikawa [28]	photo-nuclear	SUS with crater	D_2O liq.	4	1×10^{20}	0.03	1.7×10^7	4.3×10^6
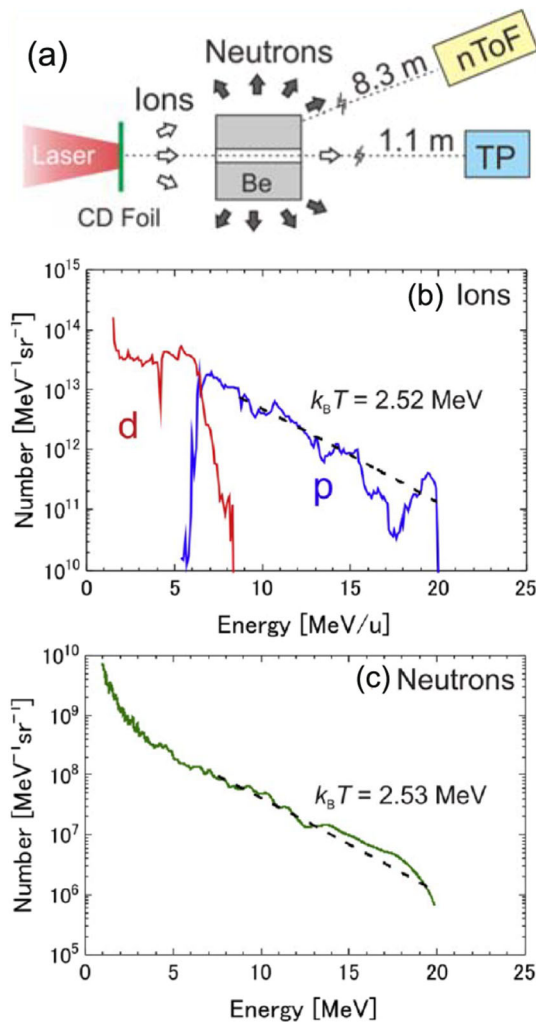
Fig. 2 a A schematic picture of the laser-driven neutron source (LDNS) utilizing protons and deuterons accelerated from a foil of deuterated polystyrene as a primary target. **b** The energy spectrum of ions measured through a pinhole on the secondary target (a block of Be). **c** The neutron spectrum simultaneously measured with a time of flight method. The figures are adopted from Ref. [22]

Fig. 3 The neutron number generated per a charge of the incident ion for the secondary target sufficiently thicker than the stopping range of the incident ions [36]. The figure is adopted from Ref. [3]
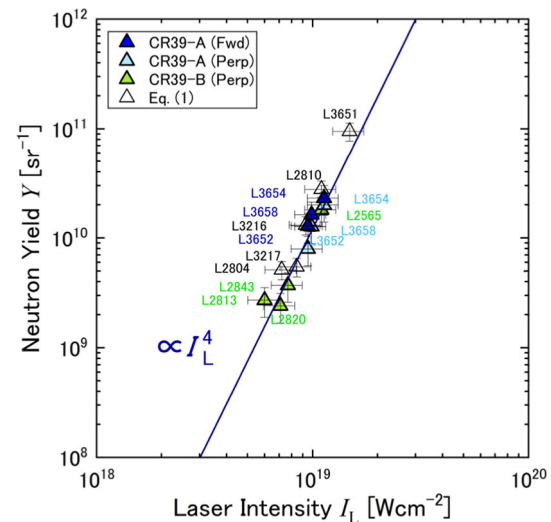
Fig. 4 The neutron yield as a function of the laser intensity. The intensity was surveyed by changing the laser energy from 400 to 930 J and fixing the pulse duration on 1.5 ps. The secondary target was Be. The laser shot number is ascribed to the each data point. The figure is adopted from Ref. [25]

materials or structures in thickness, potentially leading to an alternative probing tool than x-rays. The fast neutrons were applied for the analysis of materials in several works [12,38]. Roth et al. [12] demonstrated the first radiographic images of high-Z metal blocks by MeV neutrons. The radiographic image of water in a PET bottle was obtained by a large aperture avalanche intensifier [38]. Dual-energy fast neutron imaging [39] was demonstrated for the identification of multi-material objects. Abe et al. [40] performed a fast neutron activation analysis using time-resolved prompt γ-rays induced by the short-pulse neutrons from the LDNS.

The high-flux pulse of neutrons in the range of keV - MeV generated form LDNSs can be a novel tool to investigate nucleosynthesis in astrophysics. The elements heavier than iron are predominantly synthesized by stellar nuclear

reactions of rapid neutron capture (the r process) [41], slow neutron capture (the s process) [42], and successive photo-disintegration reactions (the γ process) [43]. To study the r process, Habs et al. [44] theoretically proposed a method possibly leading to generate neutron-rich isotopes using nuclear fusion-fission reactions between laser-accelerated heavy ions and heavy element materials, such as ^{232}Th. Hayakawa et al. [43] proposed a method to measure the reaction cross sections in inner-stellar environments by the interactions between laser-induced high-flux γ ray and the hot plasma induced by the other high-intensity laser. Hill and Wu [45] theoretically
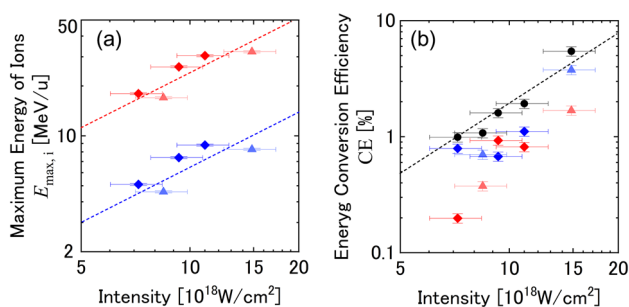
Fig. 5 The experimental results of the maximum energies of ions ($E_{\mathrm{max},i}$) (**a**) and the energy conversion efficiencies (CE) from laser to ions (**b**) as a function of the laser intensity for proton (red) and deuteron (blue). The figure is adopted from Ref. [25]
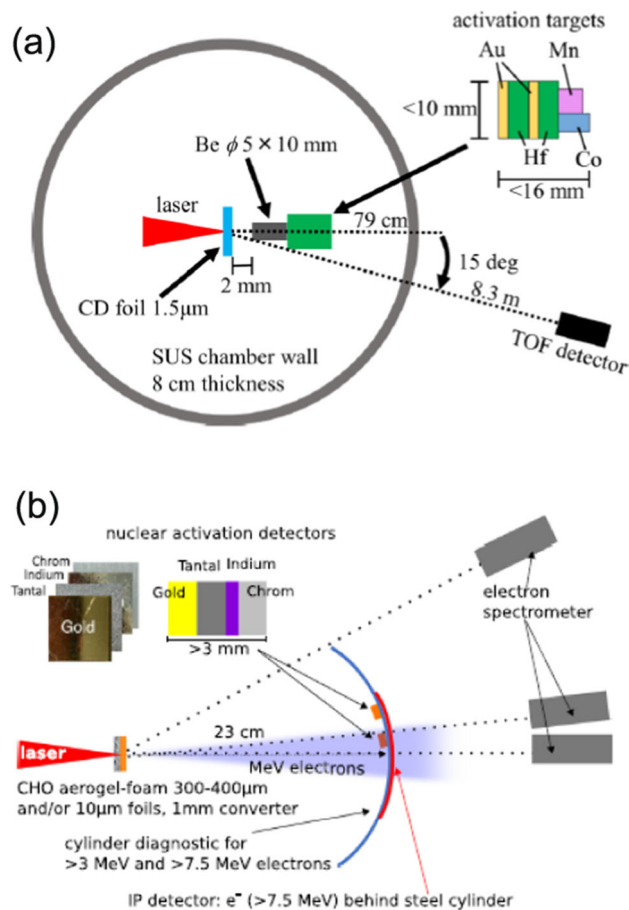

Fig. 6 The experimental setup to evaluate the high flux neutron at the vicinity of LDNS by Mori et al. [46] (**a**) and Günther et al. [27] (**b**). The figures are adopted from Ref. [27,46]

showed that neutron-rich isotopes heavier than the initial isotopes can be produced by successive capture of four neutrons, which might be achievable with the LDNS delivering 10^{12} neutrons per pulse at 1 Hz during 10^{4} s for sufficiently long-lived ($T_{1/2} > 1$ h) isotopes. The 10^{12} neutrons/pulse can soon be available even with the present LDNS at lower repetition rate.

Considering that the source size is in the order of 1 cm and the neutron pulse duration is around 1 ns at the source, the peak neutron flux reaches 10^{20} neutrons cm^{-2} s^{-1} at the vicinity of the source, which is close to the flux assumed inside burning stars. In order to evaluate the high flux neutron environments, activation method [27,46] is one of the promising methods, where the number of unstable isotopes are precisely measured. The neutron yield is evaluated by using the isotope that the production cross section is known. Mori et al. [46] employed (n, $2n$) nuclear reaction for the activation samples directly attached onto the neutron source (Fig. 6a), and evaluated the neutron yield in the energy range higher than 8 MeV. Günther et al. [27] evaluated the number of protons and neutrons by a combination of several activation channels (Fig. 6b).

3.2 Epi-thermal neutrons

The neutron produced in the converter target is usually born in the MeV region, and to use them for different applications they have to be slowed-down, known as moderation. Two basic effects are taken into account in the process of the designing a moderator: (1) neutron leakage and (2) the pulse duration. The purpose of a moderator is to induce a sufficient amount of neutron energy loss which is done via series of elastic and inelastic collisions where energy exchange between the medium and the incoming neutrons is a function of the scattering angle. Therefore many of the facilities use a compact moderator for this purpose.

The epi-thermal neutron generation was firstly demonstrated by Mirfayzi et al. [18], when a compact moderator was located behind the secondary target that generated fast neutrons. As shown in Fig. 7b, the moderator consists of 4-cm thick high density polystyrene (HDP), as the main moderation materials for the neutrons, and high Z materials as neutron reflectors.

Supported by a Monte-Carlo simulation, the fluence of epithermal neutrons were evaluated to be 10^{5} neutrons/sr/pulse in the energy range of 0.5–300 eV.

As discussed in Sect. 1, the cross sections for neutron-induced reactions exhibit the presence of resonances, which are related to excited states of the compound nucleus just above the separation threshold energy. Since these resonances appear at energies that are specific for each nuclide, they can be used to identify and quantify elements and isotopes as the basis of neutron resonance spectroscopy (NRS) [47]. The resonance structures are analyzed by the time-of-flight (ToF) technique. The energy resolution ΔE_n is determined for the neutron energy E_n by

$$\Delta E_n/E_n = 2\Delta\tau\sqrt{2E_n/m}/D, \tag{5}$$

where $\Delta\tau$ is the temporal spread by the moderator, and D is the flight distance. Hence, if LDNS can provide extremely
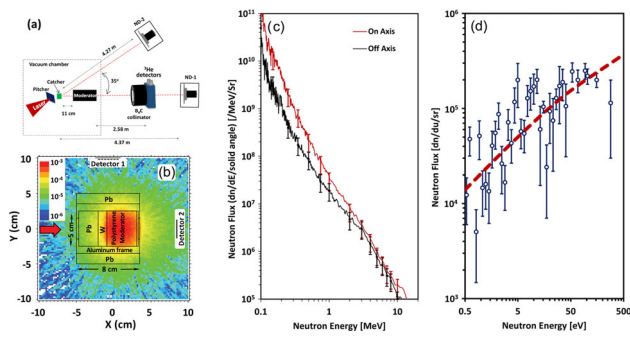
Fig. 7 a Schematic of the experimental setup. Epithermal neutrons produced by the moderator were diagnosed by the ^{3}He proportional counters employed in the ToF mode, placed behind a B_4C collimator. **b** The design of the moderator superimposed on the neutron (in the range of 1 eV–1 keV) flux distribution across the mid-plane of the moderator, obtained from the simulation for 1 MeV neutrons entering the moderator from the left side (shown by red arrow). **c** Typical spectra of fast neutrons produced in the experiment. **d** Epithermal neutron spectra produced by the moderator, averaged over 16 laser shots. The figures were adopted from Ref. [18]

short pulses of epi-thermal neutrons, it potentially leads to higher energy resolution, as discussed in the earlier works [9, 26]. Nowadays, several groups performed proof-of-principle experiments on the laser-driven NRS [24,25] using the ToF beamlines of a few meter scale, which are shorter by one order of magnitude than those at ABNF including GELINA: the linear electron accelerator facility in Geel [48] or J-PARC [49].

To evaluate the feasibility of the NRS with LDNS, Zimmer et al. [24] developed a neutron moderator and analyzed epithermal neutrons transmitted through the samples of tungsten (W) and tantalum (Ta). They measured the structures on the neutron spectrum shown in Fig. 8 with 18 accumulated laser shots. They also showed the feasibility of neutron resonance imaging (NRI) for the plates of cadmium (Cd) and indium (In) behind a 2 mm lead.

In Fig. 9, the neutron energy (E_n) was selected based on the ToF technique by gating the detector, which is shown in Fig. 13a. The radiographic images were measured for the regions of $E_n < 0.05$ eV, $0.05 < E_n < 0.1$ eV and $E_n > 0.1$ eV, where different attenuations were observed for the same sample depending on the neutron energy. It was reported that the large attenuation caused by the resonance absorption by ^{113}Cd allowed to identify the Cd within the field of view.

Yogo et al. [25] performed the laser-driven NRS with a single pulse of neutrons generated by a single laser shot. The experimental setup is shown in Fig. 10a, where the neutron detector for the ToF analysis was located 1.8 m downstream of the LDNS. In general, the neutron pulse is expanded as the moderator thickness is increased, while the number of moderated neutrons is enhanced. In order to provide sufficient resolution with the 1.8-m beamline, the moderator was
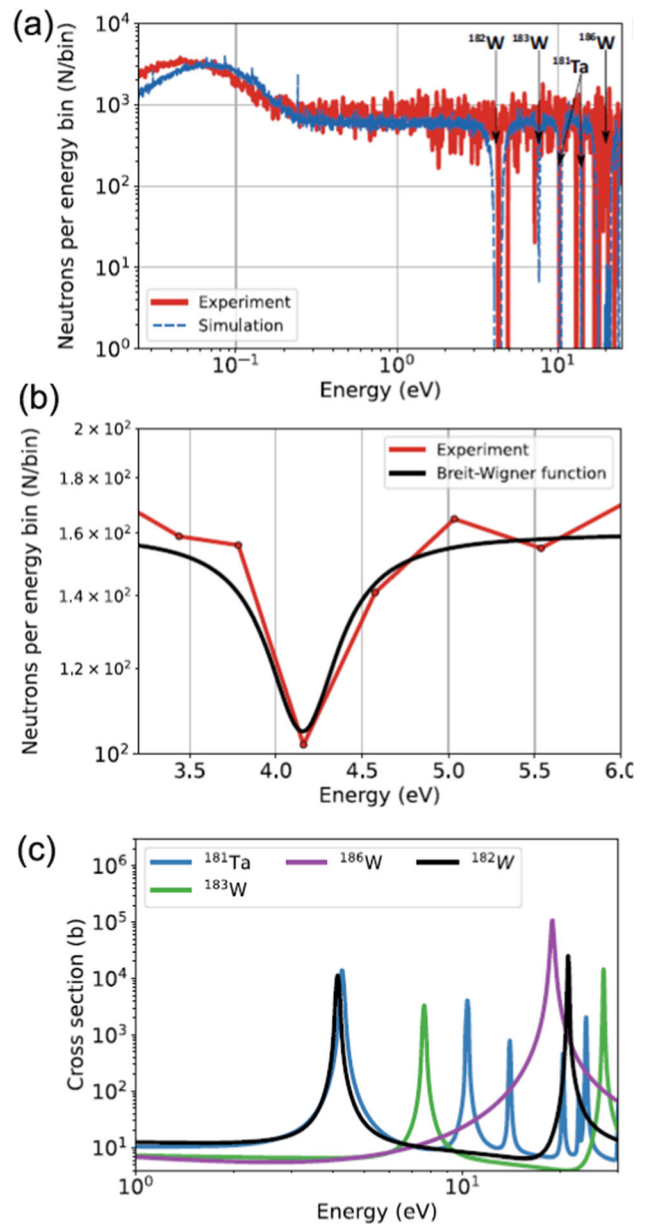

Fig. 8 a Measured neutron spectrum after transmission through a tungsten sample (red) and a Monte-Carlo simulation (blue). **b** Measured neutron flux at the ^{182}W resonance (red) with an increased bin width. The Breit–Wigner function (black) of the resonance of ^{182}W with the position of 4.15 eV and the FWHM width of 0.55 eV is in good agreement with the measurement. **c** All relevant resonances for tungsten and tantalum in the range of 1–25 eV. The figures are adopted from Ref. [24]

designed to be on a balance point between the duration and the number of epi-thermal neutrons. As shown in Fig. 10b, the Be secondary target (10 mm in thickness, 5 mm in diameter) was surrounded by the moderator made from HDP having a thickness of 30 mm. The pulse duration was estimated to be $\Delta\tau = 0.6$ μs at $E_n = 5$ eV by a Monte-Carlo simulation, where the time dispersion of the ToF detector was taken into
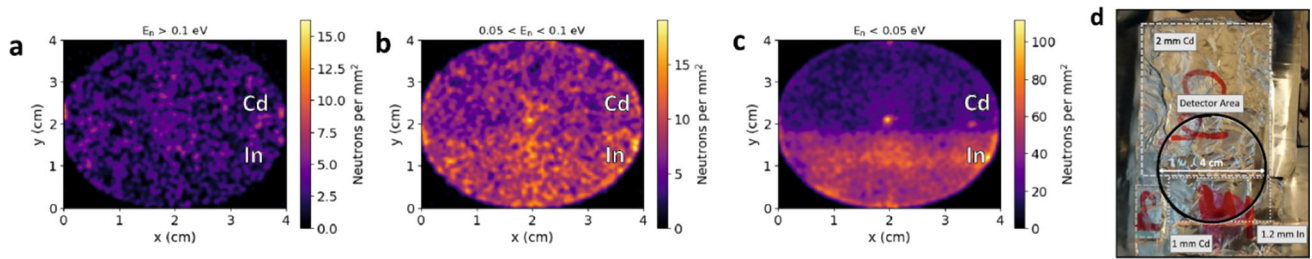
Fig. 9 Neutron resonance imaging (NRI) with a LDNS [24]. **a** The MCP detector signal shows all non-resonant neutron events with arrival times corresponding to energies > 0.1 eV. **b** The MCP detector signal shows events attributed to neutron energies between 0.05 and 0.1 eV. An increased absorption behind the 2-mm cadmium sheet is visible. **c** shows the distribution of neutron events with energies below 0.05 eV. A strong attenuation is visible behind the cadmium sheet and a small attenuation is observed behind the indium sample. **d** Sample distribution in front of the borated MCP detector. The figures are adopted from Ref. [24]
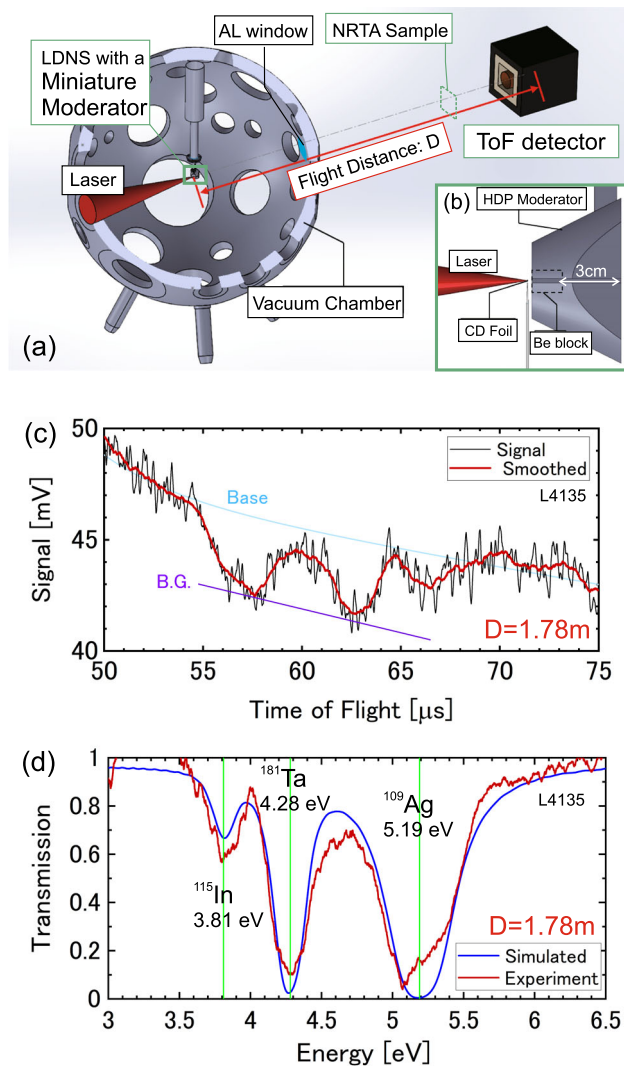
Fig. 10 **a**, **b** Schematic pictures of the NRS beamline (**a**) and the miniature moderator (**b**) installed on the LDNS. **c** The signal measured by the TOF detector for the multilayer sample of 0.1 mm thick Ag, Ta and In. **d** The comparison between experimental and simulated transmittance as a function of the neutron energy for the Ag–Ta–In multilayer sample. The figures are adopted from Ref. [25]
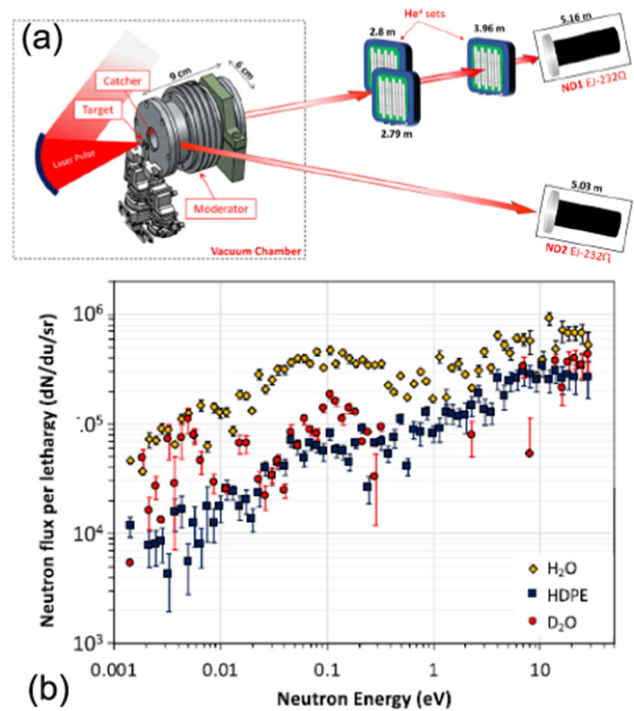

Fig. 11 **a** Schematic of the experimental setup. Multi-MeV protons were generated in proximity to the ^{7}Li catcher by irradiating the Vulcan laser on 20 μm thick Au foils. The ^{7}Li cylinder of 1 cm diameter and 2 cm length was embedded in the moderator housing to maximize coupling of fast neutrons with the moderator material. The fast and moderated neutrons were diagnosed by two scintillator-based (ND-1 and ND-2) and three sets of ^{3}He proportional detectors. **b** The background subtracted neutron spectra measured in the experiment for the H_2O moderator compared to those obtained for 4 cm thick HDP and 6 cm thick D_2O moderators. The figures are adopted from Ref. [21]

consideration together with the $\Delta\tau$. The NRS was performed for the multilayer sample of Ta, In and silver (Ag), located on the neutron path to the detector. Although the sample exhibits resonance peaks adjacent to each other, the resonance structures were identified for ^{115}In, ^{181}Ta and ^{109}Ag on the spectrum (Fig. 10d). The energy resolution was esti-

mated to be 2.3% at 5 eV, which is sufficient to identify the three resonance dips above.

3.3 Thermal neutrons

Mirfayzi et al. [21] assessed thermal neutron generation by comparing three kinds of moderator materials, light water (H_2O), heavy water (D_2O), and HDP at room temperature. A solid lithium (Li) as a secondary target was embedded in the aluminum frame of the moderator materials to enhance the collection ratio of the fast neutrons generated from the Li (Fig. 11). They used an endothermic process $^7Li(p, n)^7Be$, which was expected to efficiently generate sub-MeV neutrons by protons having energies near the reaction threshold (2.373 MeV). The neutron spectra obtained were fitted by Maxwellian distributions with a temperature of $k_B T \sim 25$ meV, which corresponds to the room temperature. The yield of thermal neutrons (< 0.5 eV) was 1.4×10^6 n/sr at maximum for the H_2O moderator, converted from the fast neutrons of $\sim 1.7 \times 10^9$ n/sr.

Yogo et al. [22] demonstrated a dual radiography using laser-driven thermal neutrons and x-ray, simultaneously. As a proof of principle, they performed non-destructive inspection for hazardous substances (Cd) for two kinds of typical batteries: a nickel (Ni)-Cd battery and a nickel-metal hydride (Ni-MH) battery. As shown in Fig. 12a, the samples were attached on the 10 cm thick HDP moderator. The fast neutrons from the LDNS were thermalized by the moderator, while x-ray was produced from the primary target and penetrate the moderator. The x-ray image (Fig. 12d) was recorded by an Imaging Plate located just downstream of the samples. The neutron image was obtained with the activation of a dysprosium (Dy) plate. ^{164}Dy (28% natural abundance) predominantly absorbs thermal neutrons via $^{164}Dy(n, \gamma)^{165}Dy$ reaction. The unstable isotope ^{165}Dy β-decays with a half-life of 2.234 h. After the exposure to the neutrons, the Dy plate was placed on the other IP for 2 h, when the β image, which corresponds to the image of thermal neutrons, was recorded (Fig. 12c). The transmittance of x-ray was similar for Ni-MH (dashed line around $x = 10$–20 in Fig. 12e) and Ni-Cd (dashed line around $x = 10$–20 in Fig. 12g). On the other hand, the neutron image showed drastically low transmittance (solid line around $x = 10$–20 in Fig. 12g) compared with that of Ni-MH (solid line around $x = 10$–20 in Fig. 12e). This is attributed to the presence of a Cd anode, which absorbs thermal neutrons. With the support of a Monte-Carlo simulation, the Cd anode thickness was evaluated from the transmittance to be 0.76 mm, in agreement with the value of the product data sheet.

Similarly, Zimmer et al. [24] successfully measured a thermal neutron radiography of the sheets of In and cadmium (Cd) behind a lead plate (Fig. 13). The imaging detector was gated to measure the neutrons with energies between 10 meV and 2 eV, base on the ToF technique. In Fig. 13c, the attenuation was stronger for the sheet of Cd, distinguished from the In sheet. The sample thickness was successfully evaluated by the neutron attenuation measured on the image and known cross sections of the reactions.

Wei et al. [23] demonstrated a radiography of water with thermal neutrons and x-ray (Fig. 14a) at the same laser shot with the NRS measurement [25] mentioned in the previous section. The water was filled in a 1 mm thick stainless pipe, and an empty pipe was put together as a reference. In the x-ray image (Fig. 14c) shadow of two pipes was monitored by the IP. The neutron image (Fig. 14b), detected by the Dy activation method, clearly showed high transmittance for the empty pipe (Fig. 14e).

3.4 Cold neutrons

Mirfayzi et al. [20] developed a moderator to generate cold neutrons (< 5 meV) for the first time (Fig. 15a). A copper cell was cryogenic cooled down to 11 K and filled with solid hydrogen and located downstream at a 5 cm distance from the LDNS.

The neutrons were cooled down by the solid hydrogen moderator and analyzed by He-3 proportional counters located on axis at 3.28 m distance, based on the ToF technique (Fig. 15b). The cold neutron flux of 2×10^3 n/cm^2 was obtained by a single laser shot at the vicinity of the moderator surface. The pulse duration of hundreds of ns was evaluated for neutron energies down to meV with a Monte-Carlo simulation. The short pulse duration was attributed to the small size (4 cm) of the solid hydrogen moderator.

4 Discussion and future prospects

Here, we recall the features of LDNS discussed in the introduction: (i) compactness of the source, (ii) neutron pulse shortness and (iii) transportability of laser beam. After reviewing the activities oriented to applications in the previous section, we additionally find the other features of LDNS: (iv) capability of *single shot* analysis, and (v) *multi-beam* availability, such as x-ray and electron, simultaneously with the neutrons.

The radiographic images shown in Figs. 12 [22], 13 [24], and 14 [23] were measured by a single pulse of neutrons generated by a single shot of the laser. The neutron density was $\sim 10^5$ neutrons/cm^2 [wei] on the imaging device at 10 cm distance from the moderator surface. Considering the moderation process, the duration of thermal neutrons is in the order of 1–10 μs. This fact indicates that LDNS can provide "snap shot" images of neutrons for high-speed phenomena or moving objects. In addition, the ps pulse of x-ray is generated in synchronization with the neutron pulse *automatically*,
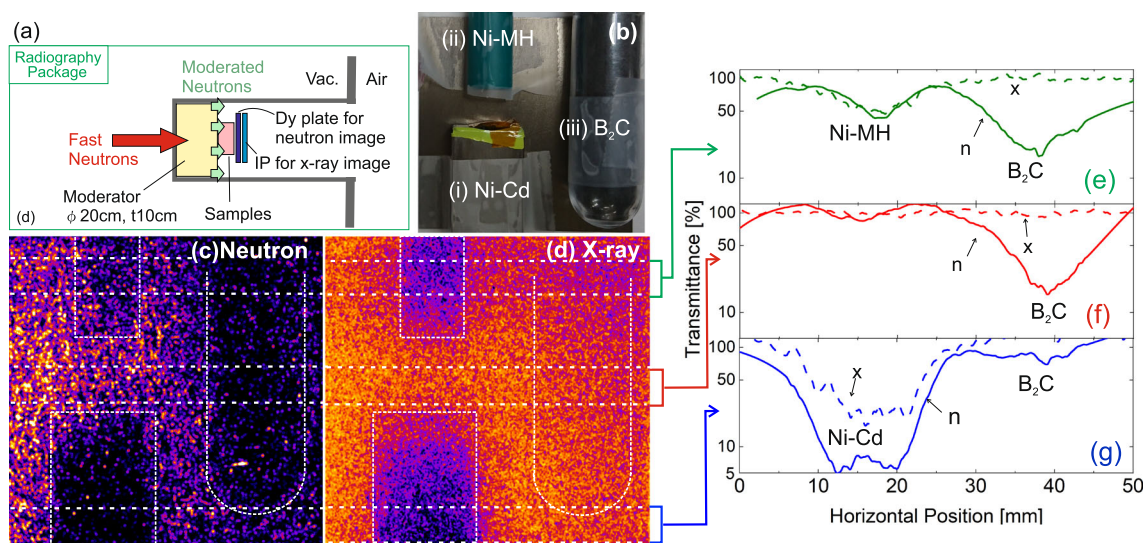
Fig. 12 a Schematic of thermal neutron radiography located downstream of the LDNS shown in Fig. 2(a). **b** The picture of samples. **c**, **d** Radiographic images of (i) a nickel–cadmium (Ni–Cd) battery, (ii) a nickel-metal hydride battery, and (iii) boron carbide (B$_2$C) powder as a reference obtained with neutrons (**c**) and x-rays (**d**). **e**–**g** The transmit-

tance of neutrons (solid) and x-rays (dashed) along the horizontal lines indicated in green, red and blue belts, respectively, seen in (**c**), (**d**). The results **c** and **d** were obtained simultaneously with a single laser shot. The figure is adopted from Ref. [22]
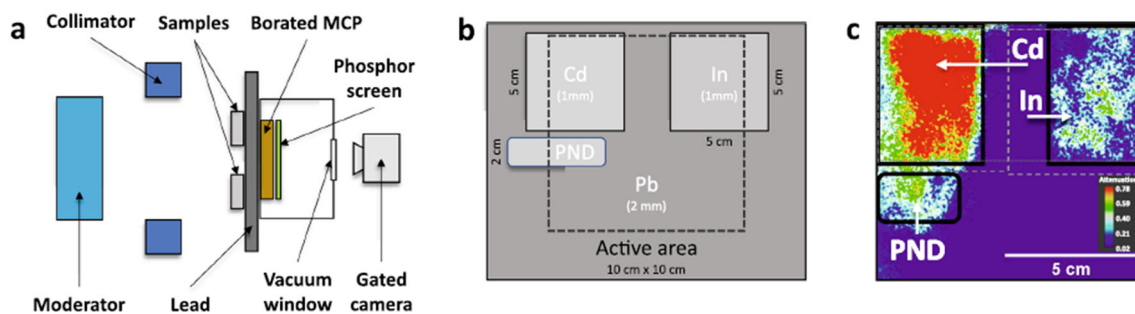
Fig. 13 a Schematic setup of the thermal radiography measurement (top view) developed by Zimmer et al. [24]. **b** Sample distribution across the detector (front view). One millimeter cadmium (Cd) and In sheets

are placed behind a 2-mm lead plate. **c** Thermal neutron radiography of the sample. The figure is adopted from Ref. [24]

allowing to observe high Z materials in synchronization with hydrogen-rich materials. It was reported [23] that LDNS can be utilized for the non-destructive inspection of metal pipes filled with 82 MPa hydrogen gas, which is assumed in future hydrogen storage or transportation system.

As shown in Fig. 10, elements or isotopes of high Z materials were identified in NRS with the 1.8 m beamline by the single laser shot [25]. The neutron density was 10^{2-3} neutrons/cm^2 at the detector surface for $1 \leq E_n \leq 20$ eV in the single shot. On the other hand, in GELINA [48], as a typical ABNF, NRS is preformed with the neutron flux of $\sim 10^3$ neutrons/cm^2/s for $1 \leq E_n \leq 20$ eV with 800 Hz at a distance of 20 m from the source. Assuming that the neutron density reduces as the square of the distance, the single shot analysis was enabled by the short distance from the source, as

a benefit of the pulse shortness of the moderated neutrons. In addition, the single neutron pulse reached the detector within the duration of sub-µs in the laser-driven NRS [25]. This fact leads to bring high temporal resolution for NRS. Especially, the Doppler broadening of the resonance structure is utilized for neutron thermometer [50–52] in ABNF. As discussed in [25] the short acquisition time of the laser-driven NRS may enable a *real-time* neutron thermometer for objects in operation, including blue-light-emitting diodes (LED), batteries and semiconductor power devices.

The proton acceleration in the order of 100 MeV is expected at ELI-NP [53]. It was reported [36] that the number of neutrons generated until the incident proton is stopped in the secondary target increases as the square of the proton energy. The newly commissioned multi-PW facilities will

Fig. 14 **a** Radiography experimental setup by laser-driven low energy neutron source. The radiography set is set at a distance of 10 cm from the source. The Dy plate and IP were used to record neutron and x-ray signals, respectively. **b** Measured neutron radiography image. **c** X-ray image. **d** Transmittance for neutron (red) and x ray (blue) along the horizontal position obtained from the images of (**c**) and (**d**). The figure is adopted from Ref. [23]
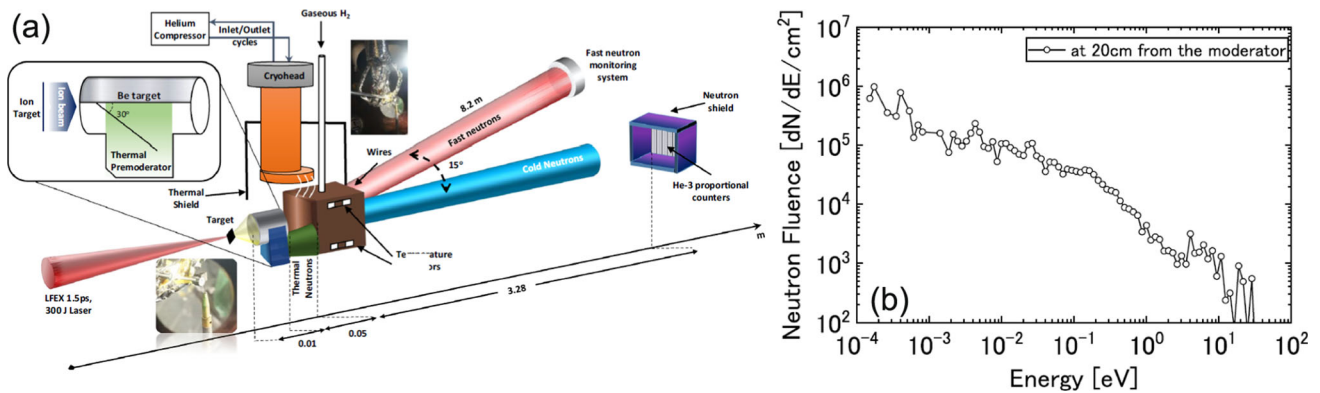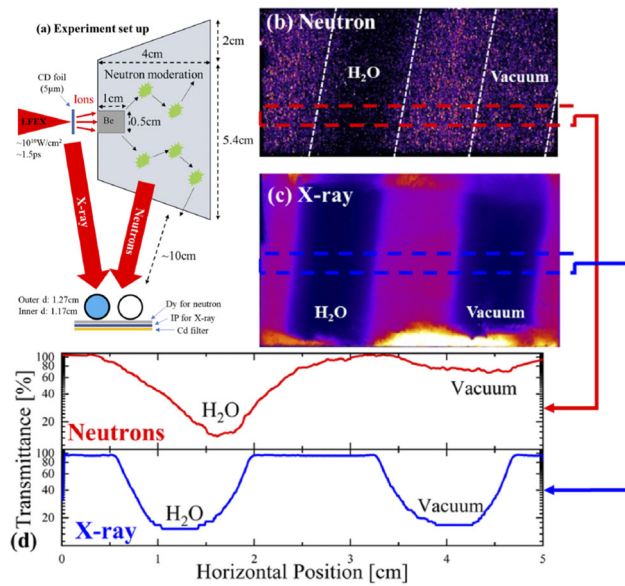

Fig. 15 **a** The setup for laser-driven cold neutron generation by cryogenic cooled solid hydrogen moderator. **b** Thermal/cold neutron spectrum from the cryogenic moderator, where the unit of the vertical axis is n/eV/cm^2/pulse. The figure is adopted from Ref. [20]

deliver game-changing results on the laser-driven neutron generation and its application. Activities to maximize the potential of LDNS will pave the way for bringing neutrons to areas that have never benefited from neutron science.

Data Availability Statement This manuscript has no associated data or the data will not be deposited. [Authors' comment: Data sharing is not applicable to this article as no data sets were generated or analyzed during the current study.]

References

1. W.P. Leemans, B. Nagler, A.J. Gonsalves, C. Toth, K. Nakamura, C.G.R. Geddes, E. Esarey, C.B. Schroeder, S.M. Hooker, Nat. Phys. **2**, 696 (2006)
2. A. Higginson, R.J. Gray, M. King, R.J. Dance, S.D. Williamson, N.M. Butler, R. Wilson, R. Capdessus, C. Armstrong, J.S. Green, S.J. Hawkes, P. Martin, W.Q. Wei, S.R. Mirfayzi, X.H. Yuan, S. Kar, M. Borghesi, R.J. Clarke, D. Neely, P. McKenna, Nat. Commun. **9**, 724 (2018)
3. K. Mima, A. Yogo, S.R. Mirfayzi, Z. Lan, Y. Arikawa, Y. Abe, H. Nishimura, Appl. Opt. **61**, 2398 (2022)
4. H. Daido, M. Yamanaka, K. Mima, K. Nishihara, S. Nakai, Y. Kitagawa, E. Miura, C. Yamanaka, A. Hasegawa, Appl. Phys. Lett. **51**, 2195 (1987)
5. M. Key, M. Cable, T. Cowan, K. Estabrook, B. Hammel, S. Hatchett, E. Henry, D. Hinkel, J. Kilkenny, J. Koch, W. Kruer, A.B. Langdon, B. Lasinski, R. Lee, B. Macgowan, A.J. MacKinnon, J. Moody, M. Moran, A.A. Offenberger, D. Pennington, M. Perry, T. Phillips, T. Sangster, M. Singh, M. Stoyer, M. Tabak, G. Tietbohl, M. Tsukamoto, K. Wharton, S. Wilks, Phys. Plasmas **5**, 1966 (1998)
6. T. Ditmire, J. Zweiback, V.P. Yanovsky, T.E. Cowan, G. Hays, Nature **398**, 489–492 (1999)
7. K.L. Lancaster, S. Karsch, H. Habara, F.N. Beg, E.L. Clark, R. Freeman, M.H. Key, J.A. King, R. Kodama, K. Krushelnick, K.W.D. Ledingham, P. McKenna, C.D. Murphy, P.A. Norreys, R. Stephens, C. Stoeckl, Y. Toyama, M.S. Wei, M. Zepf, Phys. Plasmas **11** (2004)
8. D.P. Higginson, J.M. McNaney, D.C. Swift, T. Bartal, D.S. Hey, R. Kodama, S.L. Pape, A. MacKinnon, D. Mariscal, H. Nakamura, N. Nakanii, K.A. Tanaka, F.N. Beg, Phys. Plasmas **17**, 100701 (2010)
9. D.P. Higginson, J.M. McNaney, D.C. Swift, G.M. Petrov, J. Davis, J.A. Frenje, L.C. Jarrott, R. Kodama, K.L. Lancaster, A.J. MacKinnon, H. Nakamura, P.K. Patel, G. Tynan, F.N. Beg, Phys. Plasmas (2011). https://doi.org/10.1063/1.3654040
10. L. Willingale, P.M. Nilson, A.G.R. Thomas, S.S. Bulanov, A. Maksimchuk, W. Nazarov, T.C. Sangster, C. Stoeckl, K. Krushelnick, Phys. Plasmas (2011). https://doi.org/10.1063/1.3563438
11. D. Jung, K. Falk, N. Guler, O. Deppert, M. Devlin, A. Favalli, J.C. Fernandez, D.C. Gautier, M. Geissel, R. Haight, C.E. Hamilton, B.M. Hegelich, R.P. Johnson, F. Merrill, G. Schaumann, K. Schoenberg, M. Schollmeier, T. Shimada, T. Taddeucci, J.L. Tybo, S.A. Wender, C.H. Wilde, G.A. Wurden, M. Roth, Phys. Plasmas (2013). https://doi.org/10.1063/1.4804640
12. M. Roth, D. Jung, K. Falk, N. Guler, O. Deppert, M. Devlin, A. Favalli, J. Fernandez, D. Gautier, M. Geissel, R. Haight, C.E. Hamilton, B.M. Hegelich, R.P. Johnson, F. Merrill, G. Schaumann, K. Schoenberg, M. Schollmeier, T. Shimada, T. Taddeucci, J.L. Tybo, F. Wagner, S.A. Wender, C.H. Wilde, G.A. Wurden, Phys. Rev. Lett. **110**, 1 (2013)
13. C. Zulick, F. Dollar, V. Chvykov, J. Davis, G. Kalinchenko, A. Maksimchuk, G.M. Petrov, A. Raymond, A.G. Thomas, L. Willingale, V. Yanovsky, K. Krushelnick, Appl. Phys. Lett. **102**, 124101 (2013)
14. A. Maksimchuk, A. Raymond, F. Yu, G.M. Petrov, F. Dollar, L. Willingale, C. Zulick, J. Davis, K. Krushelnick, Appl. Phys. Lett. (2013). https://doi.org/10.1063/1.4807143
15. M. Storm, S. Jiang, D. Wertepny, C. Orban, J. Morrison, C. Willis, E. Mccary, P. Belancourt, J. Snyder, W. Bang, E. Gaul, G. Dyer, T. Ditmire, R.R. Freeman, K. Akli, M. Storm, S. Jiang, D. Wertepny, C. Orban, J. Morrison, C. Willis, E. Mccary, Phys. Plasmas **20**, 053106 (2013)
16. S. Kar, H. Ahmed, R. Prasad, M. Cerchez, S. Brauckmann, B. Aurand, G. Cantono, P. Hadjisolomou, C.L.S. Lewis, A. Macchi, G. Nersisyan, A.P.L. Robinson, A.M. Schroer, M. Swantusch, M. Zepf, O. Willi, M. Borghesi, Nat. Commun. **7**, 10792 (2016)
17. A. Alejo, A.G. Krygier, H. Ahmed, J.T. Morrison, R.J. Clarke, J. Fuchs, A. Green, J.S. Green, D. Jung, A. Kleinschmidt, Z. Najmudin, H. Nakamura, P. Norreys, M. Notley, M. Oliver, M. Roth, L. Vassura, M. Zepf, M. Borghesi, R.R. Freeman, S. Kar, Plasma Phys. Control. Fusion **59**, 064004 (2017)
18. S.R. Mirfayzi, A. Alejo., H. Ahmed, D. Raspino, S. Ansell, L.A. Wilson, C. Armstrong, N.M.H. Butler, R.J. Clarke, A. Higginson, J. Kelleher, C.D. Murphy, M. Notley, D.R. Rusby, E. Schooneveld, M. Borghesi, P. Mckenna, N.J. Rhodes, D. Neely, C.M. Brenner, S. Kar, Appl. Phys. Lett. **111**, 044101 (2017)
19. A. Kleinschmidt, V. Bagnoud, O. Deppert, A. Favalli, S. Frydrych, J. Hornung, D. Jahn, G. Schaumann, F. Wagner, G. Wurden, B. Zielbauer, M. Roth, A. Kleinschmidt, V. Bagnoud, O. Deppert, A. Favalli, S. Frydrych, J. Hornung, D. Jahn, G. Schaumann, A. Tebartz, F. Wagner, G. Wurden, B. Zielbauer, M. Roth, Phys. Plasmas **25**, 053101 (2018)
20. S.R. Mirfayzi, A. Yogo, Z. Lan, T. Ishimoto, A. Iwamoto, M. Nagata, M. Nakai, Y. Arikawa, Y. Abe, D. Golovin, Y. Honoki, T. Mori, K. Okamoto, S. Shokita, D. Neely, S. Fujioka, K. Mima, H. Nishimura, R. Kodama, Sci. Rep. **10**, 20157 (2020)
21. S.R. Mirfayzi, H. Ahmed, D. Doria, A. Alejo, S. Ansell, R.J. Clarke, B. Gonzalez-Izquierdo, P. Hadjisolomou, R. Heathcote, T. Hodge, P. Martin, D. Raspino, E. Schooneveld, P. McKenna, N.J. Rhodes, D. Neely, M. Borghesi, S. Kar, Appl. Phys. Lett. **116**, 174102 (2020)
22. A. Yogo, S.R. Mirfayzi, Y. Arikawa, Y. Abe, T. Wei, T. Mori, Z. Lan, Y. Hoonoki, D.O. Golovin, K. Koga, Y. Suzuki, M. Kanasaki, S. Fujioka, M. Nakai, T. Hayakawa, K. Mima, H. Nishimura, S. Kar, R. Kodama, Appl. Phys. Express **14**, 106001 (2021)
23. T. Wei, A. Yogo, T. Hayakawa, Y. Arikawa, Y. Abe, M. Nakanishi, S.R. Mirfayzi, Z. Lan, T. Mori, K. Mima, S. Fujioka, M. Murakami, M. Nakai, H. Nishimura, S. Kar, R. Kodama, AIP Adv. **12**, 045220 (2022)
24. M. Zimmer, S. Scheuren, A. Kleinschmidt, N. Mitura, A. Tebartz, G. Schaumann, T. Abel, T. Ebert, M. Hesse, S. Zahter, S.C. Vogel, O. Merle, R.J. Ahlers, S.D. Pinto, M. Peschke, T. Kroll, V. Bagnoud, C. Rodel, M. Roth, Nat. Commun. (2022). https://doi.org/10.1038/s41467-022-28756-0
25. A. Yogo, Z. Lan, Y. Arikawa, Y. Abe, S.R. Mirfayzi, T. Wei, T. Mori, D. Golovin, T. Hayakawa, N. Iwata, S. Fujioka, M. Nakai, Y. Sentoku, K. Mima, M. Murakami, M. Koizumi, F. Ito, J. Lee, T. Takahashi, K. Hironaka, S. Kar, H. Nishimura, R. Kodama, Phys. Rev. X **13**, 011011 (2023)
26. I. Pomerantz, E. McCary, A.R. Meadows, A. Arefiev, A.C. Bernstein, C. Chester, J. Cortez, M.E. Donovan, G. Dyer, E.W. Gaul, D. Hamilton, D. Kuk, A.C. Lestrade, C. Wang, T. Ditmire, B.M. Hegelich, Phys. Rev. Lett. **113**, 1 (2014)
27. M.M. Gunther, O.N. Rosmej, P. Tavana, M. Gyrdymov, A. Skobliakov, A. Kantsyrev, S. Zahter, N.G. Borisenko, A. Pukhov, N.E. Andreev, Nat. Commun. **13**, 170 (2022)
28. Y. Arikawa, A. Morace, Y. Abe, N. Iwata, Y. Sentoku, A. Yogo, K. Matsuo, M. Nakai, H. Nagatomo, K. Mima, H. Nishimura, S. Fujioka, R. Kodama, S. Inoue, M. Hashida, S. Sakabe, D. De Luis, G. Gatti, M. Huault, J.A. Pérez-Hernández, L. Roso, L. Volpe, Phys. Rev. Res. **5**, 013062 (2023)
29. A.B. Zylstra, O.A. Hurricane, D.A. Callahan, A.L. Kritcher, J.E. Ralph, H.F. Robey, J.S. Ross, C.V. Young, K.L. Baker, D.T. Casey, T. Doppner, L. Divol, M. Hohenberger, S.L. Pape, A. Pak, P.K. Patel, R. Tommasini, S.J. Ali, P.A. Amendt, L.J. Atherton, B. Bachmann, D. Bailey, L.R. Benedetti, L.B. Hopkins, R. Betti, S.D. Bhandarkar, J. Biener, R.M. Bionta, N.W. Birge, E.J. Bond, D.K. Bradley, T. Braun, T.M. Briggs, M.W. Bruhn, P.M. Celliers, B. Chang, T. Chapman, H. Chen, C. Choate, A.R. Christopherson, D.S. Clark, J.W. Crippen, E.L. Dewald, T.R. Dittrich, M.J.

Edwards, W.A. Farmer, J.E. Field, D. Fittinghoff, J. Frenje, J. Gaffney, M.G. Johnson, S.H. Glenzer, G.P. Grim, S. Haan, K.D. Hahn, G.N. Hall, B.A. Hammel, J. Harte, E. Hartouni, J.E. Heebner, V.J. Hernandez, H. Herrmann, M.C. Herrmann, D.E. Hinkel, D.D. Ho, J.P. Holder, W.W. Hsing, H. Huang, K.D. Humbird, N. Izumi, L.C. Jarrott, J. Jeet, O. Jones, G.D. Kerbel, S.M. Kerr, S.F. Khan, J. Kilkenny, Y. Kim, H.G. Kleinrath, V.G. Kleinrath, C. Kong, J.M. Koning, J.J. Kroll, M.K. Kruse, B. Kustowski, O.L. Landen, S. Langer, D. Larson, N.C. Lemos, J.D. Lindl, T. Ma, M.J. Mac-Donald, B.J. MacGowan, A.J. Mackinnon, S.A. MacLaren, A.G. MacPhee, M.M. Marinak, D.A. Mariscal, E.V. Marley, L. Masse, K. Meaney, N.B. Meezan, P.A. Michel, M. Millot, J.L. Milovich, J.D. Moody, A.S. Moore, J.W. Morton, T. Murphy, K. Newman, J.M.D. Nicola, A. Nikroo, R. Nora, M.V. Patel, L.J. Pelz, J.L. Peterson, Y. Ping, B.B. Pollock, M. Ratledge, N.G. Rice, H. Rinderknecht, M. Rosen, M.S. Rubery, J.D. Salmonson, J. Sater, S. Schiaffino, D.J. Schlossberg, M.B. Schneider, C.R. Schroeder, H.A. Scott, S.M. Sepke, K. Sequoia, M.W. Sherlock, S. Shin, V.A. Smalyuk, B.K. Spears, P.T. Springer, M. Stadermann, S. Stoupin, D.J. Strozzi, L.J. Suter, C.A. Thomas, R.P. Town, E.R. Tubman, P.L. Volegov, C.R. Weber, K. Widmann, C. Wild, C.H. Wilde, B.M.V. Wonterghem, D.T. Woods, B.N. Woodworth, M. Yamaguchi, S.T. Yang, G.B. Zimmerman, Nature **601**, 542 (2022)

30. D. Strickland, G. Mourou, Opt. Commun. **55**, 447 (1985)
31. R.A. Snavely, M.H. Key, S.P. Hatchett, I.E. Cowan, M. Roth, T.W. Phillips, M.A. Stoyer, E.A. Henry, T.C. Sangster, M.S. Singh, S.C. Wilks, A. MacKinnon, A. Offenberger, D.M. Pennington, K. Yasuike, A.B. Langdon, B.F. Lasinski, J. Johnson, M.D. Perry, E.M. Campbell, Phys. Rev. Lett. **85**, 2945 (2000)
32. E.L. Clark, K. Krushelnick, M. Zepf, F.N. Beg, M. Tatarakis, A. Machacek, M.I.K. Santala, I. Watts, P.A. Norreys, A.E. Dangor, Phys. Rev. Lett. **85**, 1654 (2000)
33. A. Maksimchuk, S. Gu, K. Flippo, D. Umstadter, Phys. Rev. Lett. **84**, 4108 (2000)
34. S.C. Wilks, A.B. Langdon, T.E. Cowan, M. Roth, M. Singh, S. Hatchett, M.H. Key, D. Pennington, A. MacKinnon, R.A. Snavely, Phys. Plasmas **8**, 542 (2001)
35. P.R. Bolton, T. Hori, H. Kiriyama, M. Mori, H. Sakaki, K. Sutherland, M. Suzuki, J. Wu, A. Yogo, Nucl. Instrum. Methods Phys. Res. Sect. A Accel. Spectrom. Detect. Assoc. Equip. **620**, 71 (2010)
36. I.S. Anderson, C. Andreani, J.M. Carpenter, G. Festa, G. Gorini, C.K. Loong, R. Senesi, Phys. Rep. **654**, 1 (2016)
37. A. Yogo, K. Mima, N. Iwata, S. Tosaki, A. Morace, Y. Arikawa, S. Fujioka, T. Johzaki, Y. Sentoku, H. Nishimura, A. Sagisaka, K. Matsuo, N. Kamitsukasa, S. Kojima, H. Nagatomo, M. Nakai, H. Shiraga, M. Murakami, S. Tokita, J. Kawanaka, N. Miyanaga, K. Yamanoi, T. Norimatsu, H. Sakagami, S.V. Bulanov, K. Kondo, H. Azechi, Sci. Rep. **7**, 42451 (2017)
38. R. Mizutani, Y. Abe, Y. Arikawa, J. Nishibata, A. Yogo, S.R. Mirfayzi, H. Nishimura, K. Mima, S. Fujioka, M. Nakai, H. Shiraga, R. Kodama, High Energy Density Phys. **36**, 100833 (2020)
39. G.J. Williams, M. Aufderheide, K.M. Champley, B.Z. Djordjevi, T. Ma, C. Ryan, R.A. Simpson, S.C. Wilks, Rev. Sci. Instrum. **93**, 093514 (2022). https://doi.org/10.1063/5.0101832
40. Y. Abe, A. Nakao, Y. Arikawa, A. Morace, T. Mori, Z. Lan, T. Wei, S. Asano, T. Minami, Y. Kuramitsu, H. Habara, H. Shiraga, S. Fujioka, M. Nakai, A. Yogo, Rev. Sci. Instrum. (2022). https://doi.org/10.1063/5.0099217
41. Y.Z. Qian, G.J. Wasserburg, Phys. Rep. **442**, 237 (2007)
42. F. Kappeler, R. Gallino, S. Bisterzo, W. Aoki, Rev. Mod. Phys. **83**, 157 (2011)
43. T. Hayakawa, N. Iwamoto, T. Shizuma, T. Kajino, H. Umeda, K. Nomoto, Phys. Rev. Lett. **93**, 1 (2004)
44. D. Habs, P.G. Thirolf, M. Gross, K. Allinger, J. Bin, A. Henig, D. Kiefer, W. Ma, J. Schreiber, Appl. Phys. B Lasers Opt. **103**, 471 (2011)
45. P. Hill, Y. Wu, Phys. Rev. C **103**, 68 (2021)
46. T. Mori, A. Yogo, T. Hayakawa, S.R. Mirfayzi, Z. Lan, Y. Abe, Y. Arikawa, D. Golovin, T. Wei, Y. Honoki, M. Nakai, K. Mima, H. Nishimura, S. Fujioka, R. Kodama, Phys. Rev. C **104**, 015808 (2021)
47. P. Schillebeeckx, A. Borella, F. Emiliani, G. Gorini, W. Kockelmann, S. Kopecky, C. Lampoudis, M. Moxon, E.P. Cippo, H. Postma, N.J. Rhodes, E.M. Schooneveld, C.V. Beveren, J. Instrum. **7**, C03009 (2012)
48. B. Becker, S. Kopecky, H. Harada, P. Schillebeeckx, Eur. Phys. J. Plus (2014). https://doi.org/10.1140/epjp/i2014-14058-6
49. H. Hasemi, M. Harada, T. Kai, T. Shinohara, M. Ooi, H. Sato, K. Kino, M. Segawa, T. Kamiyama, Y. Kiyanagi, Nucl. Instrum. Methods Phys. Res. Sect. A Accel. Spectrom. Detect. Assoc. Equip. **773**, 137 (2015)
50. T. Kamiyama, H. Noda, J. Ito, H. Iwasa, Y. Kiyanagi, S. Ikeda, J. Neutron Res. **13**, 97 (2005)
51. J.C. Fernandez, C.W. Barnes, M.J. Mocko, L. Zavorka, Rev. Sci. Instrum. **90**, 094901 (2019)
52. V.W. Yuan, J.D. Bowman, D.J. Funk, G.L. Morgan, R.L. Rabie, C.E. Ragan, J.R. Quintana, H.L. Stacy, Phys. Rev. Lett. **94**, 125504 (2005)
53. K.A. Tanaka, K.M. Spohr, D.L. Balabanski, S. Balascuta, L. Capponi, M.O. Cernaianu, M. Cuciuc, A. Cucoanes, I. Dancus, A. Dhal, B. Diaconescu, D. Doria, P. Ghenuche, D.G. Ghita, S. Kisyov, V. Nastasa, J.F. Ong, F. Rotaru, D. Sangwan, P.A. Soderstrom, D. Stutman, G. Suliman, O. Tesileanu, L. Tudor, N. Tsoneva, C.A. Ur, D. Ursescu, N.V. Zamfir, Matter Radiat. Extremes **5**, 024402 (2020)